# Hydrothermally hollow $SnO_2$ microspheres as sodium ion battery anode with high capacity and superior stability

*Hong He[1,2], Maowen Xu[1,2], Jingang Yang[1,2], Bo He[1,2], Jiale Xie[1,2,3] ✉*

[1]*Faculty of Materials and Energy, Southwest University, Chongqing 400715, People's Republic of China*
[2]*Chongqing Key Laboratory for Advanced Materials & Technologies of Clean Electrical Power Sources, Chongqing 400715, People's Republic of China*
[3]*Institute of Physics & IMN Macro Nanos (ZIK), Ilmenau University of Technology, Unterpörlitzer Strasse 38, Ilmenau 98693, Germany*
✉ *E-mail: jialexie@swu.edu.cn*

Published in Micro & Nano Letters; Received on 4th May 2017; Accepted on 7th June 2017

Hollow $SnO_2$ microspheres were synthesised through a hydrothermal process with post-calcination in air. Compared with commercial $SnO_2$ nanoparticles, this organised and hollow $SnO_2$ microspheres show a 3.3–3.6 times higher charge/discharge capacity, a superior cycling stability and a higher Coulomb efficiency when used as an anode material for sodium ion batteries (SIBs). The superior performance of hollow $SnO_2$ microspheres was mainly attributed to the hollow structure with number of smaller nanoparticles. Compared with the disordered commercial $SnO_2$ nanoparticles, the organised and hollow $SnO_2$ microspheres with mesopores and micropores not only can facilitate charge transfer between the electrode and electrolyte, improve electronic and ionic transports, but also can accommodate the volume change to enhance the cycling stability of $SnO_2$-based SIB anodes. This work also demonstrates that the unique hollow structures can be broadly used to construct electrode nanomaterials.

**1. Introduction:** Due to the high availability of sodium sources, sodium ion batteries (SIBs) have recently gained great interest as a low-cost alternative to lithium-ion batteries for large-scale electric storage applications [1–5]. However, there is a limited choice of electrode materials that can accommodate or allow for reversible insertion–extraction process of Na ions. In the past decade, a large variety of materials have been developed as sodium storage cathodes, such as sodium transition metal oxides, polyanion fluorophosphates, hexacyanoferrate, sulphates, organic polymers and so on [6, 7]. These studies demonstrated that some SIBs cathode materials showed excellent performances comparable to their lithium-ion battery counter-parts [8–11].

Whereas, compared with the cathodes, less attention has been given to the anode of SIBs. Searching anodes with excellent insertion–extraction process of Na ions has become a major issue for the successful development of commercial SIBs, and extensive efforts have been devoted to the development of it [12]. Alcantara reported that hard carbon can deliver a capacity of up to 300 mAh $g^{-1}$ because Na ions can absorb onto the surfaces of nanopores [13]. However, Na-intercalated hard carbon ($Na_xC$) has higher reactivity with the non-aqueous electrolyte than that of $Li_xC_6$, raising new concerns about the stability of the electrolyte [14, 15].

Tin-based materials deserve special attention as they offer a promising alternative to carbon as anode materials due to their high theoretical capacity (Sn: 847 mAh $g^{-1}$, $SnO_2$: 667 mAh $g^{-1}$, as compared to 372 mAh $g^{-1}$ for graphite). Recently, there are reports that SnSb/C, Sn nanorods with a unique core shell structure, $SnO_2$ nanowires as an anode material for SIBs can reversibly alloy with Na, providing a good cycling stability and rate capability [16–18]. On the basis of theoretical calculation, Sn can electrochemically react with sodium to yield a final alloy $Na_{15}Sn_4$, corresponding to a theoretical capacity of 847 mAh $g^{-1}$. These studies clearly demonstrated that Sn or Sn oxides are suitable attractive anode materials for Na-ion batteries [19–22]. Still, to date, there have been very limited experimental studies on Sn and Sn oxides for reversible Na ion insertion.

Herein, hollow $SnO_2$ microspheres were synthesised simply by a hydrothermal method with post-calcination at 450°C in air for a anode of sodium ion batteries. Due to the unique architecture, the hollow $SnO_2$ micro-spheres show the higher $Na^+$ storage capacities and better electrochemical characteristics than that of commercial $SnO_2$ used.

## 2. Experimental section

2.1. Synthesis of $SnO_2$ microspheres: Initially, 4.207 g $SnCl_4 \cdot 5H_2O$ dissolved in 24 ml deionised water was used as the precursor. Then 2.738 g glucose was added into above solution with stirring for several minutes. After that the mixture was transferred into a 50 ml Teflon-lined stainless steel autoclave, sealed and maintained at 160°C for 12 h, and then cooled down to room temperature naturally. The precipitates were separated by centrifugation and washed several times with deionised water and absolute ethyl alcohol and freeze-dried to obtain the composite. In synthetic procedures, glucose plays the role of the carbon source in the hydrothermal process. The powder was then annealed at 450°C for 4 h in dry air. The black sediment turned white indicating the successful removal of carbon by oxidisation in air (hollow $SnO_2$ micro-spheres). The commercial $SnO_2$ powder (200 mesh) was bought from Aladdin Co. (China), and milled for 1 h in a shaking miller (QM-3C).

2.2. Material characterisations: Scanning electron microscope (SEM) and transmission electron microscope (TEM) testings were performed on JSM-6610 and JEM-2010 electro-microscopes, respectively. X-ray diffraction (XRD) measurements were carried out on a XRD-7000 X-ray diffractometer using Cu-Kα radiation at $\lambda = 0.154$ nm. Thermal stability was measured with a NETZSCH 409PC in dry air. The specific surface area and pore-size distribution were determined by the Brunauer–Emmett–Teller (BET) measurement by employing an ASAP-2010 surface area analyser. Raman spectra were collected by an Invia Refl (Renishaw, UK) under ambient conditions, from 2000 to 200 $cm^{-1}$ with 532.8 nm laser light.

2.3. Electrochemical characterisations: Anodes were prepared on Cu foils with slurries consisting of 80 wt% active material, 10 wt%

polyvinylidenefluoride as a binder, 10 wt% super P carbon as a conductive medium and Nmethyl-pyrrolidone as a solvent. The electrodes were then dried at 120°C for overnight in a vacuum oven. The coin type cells (CR 2032) were assembled with sodium metal as the counter electrode. 1 M $NaClO_4$ in a mixture of ethylene carbonate/propylene carbonate (in a volume ratio of 1 : 1) with 5 wt% fluoroethylene carbonate (FEC) additive as the electrolyte, and the separator was a micro-porous membrane (Celgard 2135). The cells were assembled in an argon-filled glove box. The galvanostatic charge/discharge experiments were conducted at a voltage of 0.05–2.0 V versus $Na^+/Na$ on a land system (China). Cyclic voltammogram (CV) measurements were carried out at a scan rate of 0.1 mV $s^{-1}$ using a CHI 660E electrochemical workstation. All the electrochemical tests were carried out at ambient temperature. Electrochemical impedance spectroscopy (EIS) measurements were also conducted on CHI 660E in the frequency range of 0.01–$10^5$ Hz at open circuit voltage.

**3. Results and discussion:** Figs. 1*a* and 2*a* show the XRD pattern of as-prepared hollow $SnO_2$ microspheres and commercial $SnO_2$ nanoparticles, respectively. All the main peaks in the XRD pattern (Figs. 1*a* and 2*a*) can be well indexed to the tetragonal structure (rutile type) of $SnO_2$ (JCPDS Card No. 41-1445). The nanocrystal size of hollow $SnO_2$ micro-spheres can be calculated from the average of three most intense peaks of the XRD data using the Scherrer formula

$$D = k\lambda/\beta\cos\theta \quad (1)$$

where $D$ is the mean size of the nanocrystal particles, $k$ is the dimensionless shape factor, $\beta$ is the line broadening at half maximum intensity. The average particle size of hollow $SnO_2$ microsphere is ~15.5 nm. For commercial $SnO_2$ nanoparticles, the average particle size is around 18.6 nm, which is similar as

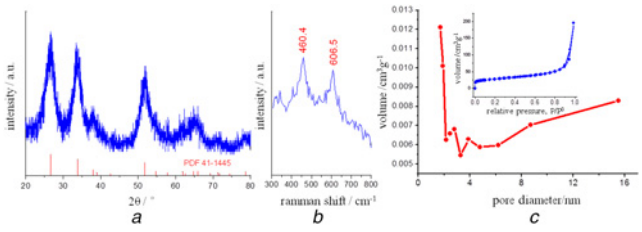


**Fig. 1** *XRD pattern, Raman spectrum, nitrogen adsorption and desorption isotherm of the hollow $SnO_2$ spheres*
*a* XRD pattern
*b* Raman spectrum
*c* Nitrogen adsorption and desorption isotherm (inset) and pore diameter distribution curve of the hollow $SnO_2$ spheres

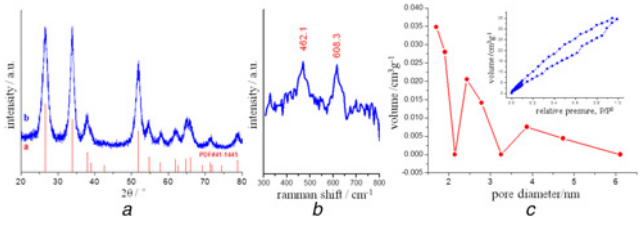


**Fig. 2** *XRD pattern, Raman spectrum, nitrogen adsorption and desorption isotherm of the commercial $SnO_2$ nanoparticles*
*a* XRD pattern
*b* Raman spectrum
*c* Nitrogen adsorption and desorption isotherm (Inset) and pore diameter distribution curve of the commercial $SnO_2$ nanoparticles

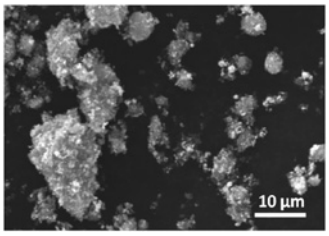


**Fig. 3** *SEM image of the commercial $SnO_2$ particles*

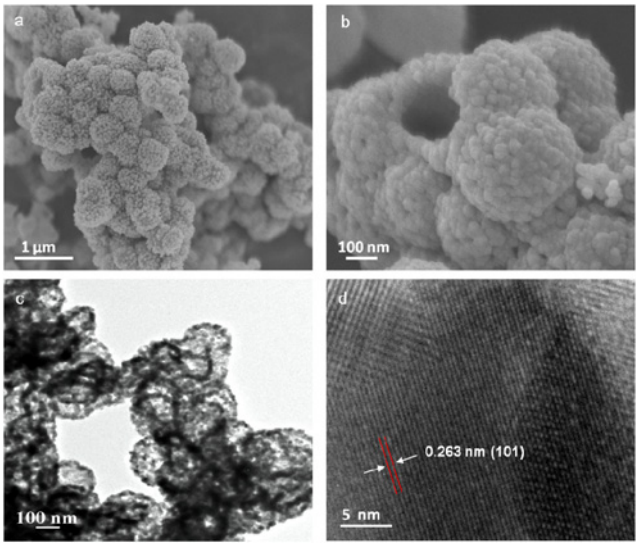


**Fig. 4** *SEM and TEM images of hollow $SnO_2$ microspheres*
*a, b* SEM image
*c, d* TEM image

that of hollow $SnO_2$ microspheres. This suggests that the commercial $SnO_2$ nanoparticles could be served as a control.

Figs. 1*b* and 2*b* show Raman spectra of the hollow $SnO_2$ microspheres and the commercial $SnO_2$ nanoparticles, respectively. Raman scattering peaks for as-prepared hollow $SnO_2$ microspheres were observed at 460.4 and 606.5 $cm^{-1}$, corresponding to the $E_g$ and $A_{1g}$ vibration modes, respectively [23]. For commercial $SnO_2$ nanoparticles, the position of these peaks is located at 462.1 and 608.3 $cm^{-1}$. The little difference can be attributed to the different synthesis methods and environments. Raman spectra further illustrate that the commercial $SnO_2$ nanoparticles are suitable as a control sample.

The porosities of the commercial $SnO_2$ nanoparticles and as-prepared hollow $SnO_2$ microspheres were measured by the nitrogen adsorption–desorption isotherms (Figs. 1*c* and 2*c*). The BET specific surface area of the hollow $SnO_2$ microspheres is 97.4 $m^2 g^{-1}$, which is 3.3 times higher than that of commercial $SnO_2$ nanoparticles (29.7 $m^2 g^{-1}$, Fig. 2*c*). The pore diameter distribution curve of hollow $SnO_2$ microspheres shows that the most probable pore diameter is about 4 nm. These mesopores facilitate the penetration of electrolyte and transportation of $Na^+$ ions. For commercial $SnO_2$ nanoparticles, the most probable pore diameter is about 3–4 nm.

In Fig. 3, the commercial $SnO_2$ nanoparticles show a disordered and aggregated morphology. Fig. 4 shows the SEM and TEM images of the as-prepared hollow $SnO_2$ microspheres. Figs. 4*a* and 4*b* exhibit a sphere shape with an average diameter of about 200–300 nm. Small grains on the shell of a sphere can be clearly observed. The average size of $SnO_2$ grains size is about 15.5 nm, which is in good agreement with the results of XRD patterns (Fig. 1*a*). In Fig. 4*b*, a break $SnO_2$ sphere can demonstrate the




doi: 10.1049/mnl.2017.0304

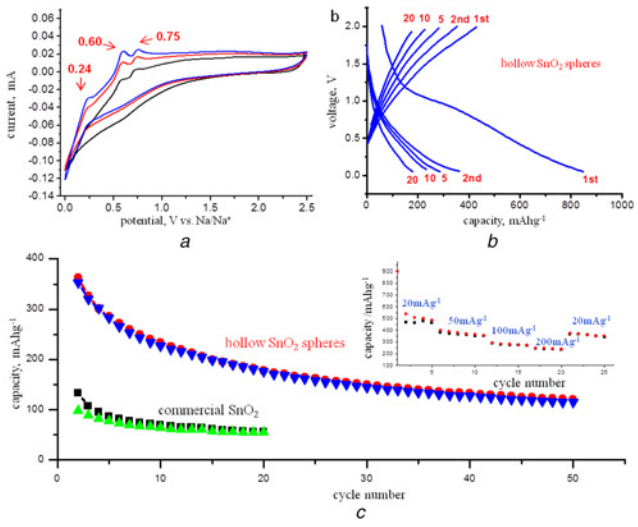


**Fig. 5** *CV curves, charge/discharge profiles and cycling performance*
*a* CV curves at a scan rate of 0.01 mV $s^{-1}$ using hollow $SnO_2$ microspheres as an anode for SIBs
*b* Charge/discharge profiles of hollow $SnO_2$ microspheres at a current density of 100 mA $g^{-1}$
*c* Cycling performance at selected cycles between 0.05 and 2.0 V at a current density of 100 mA $g^{-1}$ of hollow $SnO_2$ microspheres. Inset is the rate performance of hollow $SnO_2$ microspheres

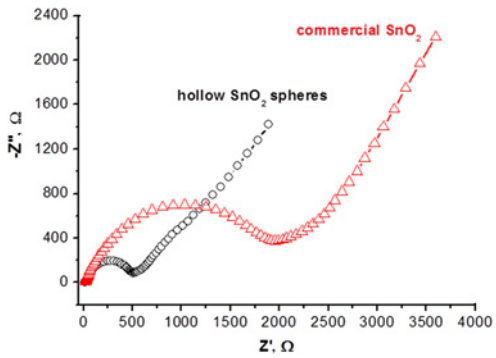


**Fig. 6** *Nyquist plots of hollow $SnO_2$ microspheres and commercial $SnO_2$ nanoparticles measured at open circuit voltage in the frequency range of 0.01–$10^5$ Hz*

hollow structure. TEM image of the hollow $SnO_2$ microspheres can further confirm that it is a hollow sphere structure (Fig. 4*c*). In Fig. 4*d*, a lattice fringe of 0.263 nm can be observed in the high-magnification TEM image of hollow $SnO_2$ microspheres, corresponding to the (101) plane of rutile $SnO_2$.

Electrochemical performances of the hollow $SnO_2$ microspheres were investigated by using coin type Na cells (Fig. 5). Fig. 5*a* shows the CV curves of hollow $SnO_2$ microsphere anodes in the first three cycles at a scan rate of 0.1 mV $s^{-1}$ between 0.05 and 2.5 V in SIBs. In the first cathodic scan, the peaks ranging from 1.0 to 0.25 V are associated with the irreversible decomposition of the electrolyte and reaction of $SnO_2$ with $Na^+$ to form $Na_xSn$ alloys embedded into the $Na_2O$ matrix [24, 25]. There are three oxidation peaks in the oxidation process that correspond to the reversible de-alloying of $Na_xSn$. The decrease of the redox peak intensities of the subsequent two cycles implies the irreversible capacity loss in the charge–discharge process, which is mainly associated with the formation of a solid-electrolyte interface (SEI) film on the electrode. The location of the three peaks remained almost unchanged during the subsequent cycles indicating good electrochemical reversibility of the hollow $SnO_2$ microsphere electrode. In an anodic scan of hollow $SnO_2$ spheres composite for SIBs, three anodic peaks at 0.24, 0.60 and 0.75 V are attributed to the desodiation of $Na_{15}Sn_4 + Na_9Sn_4$, NaSn and $NaSn_5$, respectively. The number of peaks is less than that of porous carbon/tin composite, because that the two peaks of $Na_{15}Sn_4$ and $Na_9Sn_4$ were very close and perhaps been merged in Fig. 5*a* [26, 27].

Figs. 5*b* and 5*c* show the galvanostatic charge/discharge and cycling performances of commercial $SnO_2$ nanoparticles and hollow $SnO_2$ microspheres at a constant current density of 100 mA $g^{-1}$, respectively. In the first discharge, the commercial $SnO_2$ nanoparticles and hollow $SnO_2$ microspheres deliver an initial discharge capacity of 228 and 852 mAh $g^{-1}$, respectively. However, the charge capacity of commercial $SnO_2$ nanoparticles and hollow $SnO_2$ microspheres is only 116 and 430 mAh $g^{-1}$, respectively. It suggests that both $SnO_2$ samples have almost same Coulomb efficiencies of 50% in the first charge/discharge cycle, but the hollow $SnO_2$ microspheres have totally high charge/discharge capacities due to its high specific surface area. The irreversible capacity of the first cycle mainly results from the formation of SEI and irreversible sodium insertion into $SnO_2$. Furthermore, for hollow $SnO_2$ microspheres in Fig. 5*b*, the discharge capacity retention was 363, 286, 234, 177 mAh $g^{-1}$ after 2nd, 5th, 10th, 20th cycles, respectively. On charge capacity, the charge capacity retention of hollow $SnO_2$ microsphere was 353, 282, 227, 176 mAh $g^{-1}$ after 2nd, 5th, 10th, 20th cycles, respectively. For commercial $SnO_2$ nanoparticles (Fig. 5*c*), the discharge capacity retention was 133, 87, 69, 56 mAh $g^{-1}$ after 2nd, 5th, 10th, 20th cycles, respectively. The charge capacity retention of commercial $SnO_2$ nanoparticles was 98, 78, 64, 55 mAh $g^{-1}$ after 2nd, 5th, 10th, 20th cycles, respectively. Compared with hollow $SnO_2$ microspheres, the commercial $SnO_2$ nanoparticles show rapid capacity fading with the following cycles.

To reveal the stability of hollow $SnO_2$ microspheres, the cycling performances of hollow $SnO_2$ microspheres and commercial $SnO_2$ nanoparticles based SIBs were measured at current density of 100 mA $g^{-1}$ as shown in Fig. 5*c*. The hollow $SnO_2$ microspheres have greatly higher charge/discharge capacity and superior cycling performance than that of commercial $SnO_2$ nanoparticles. Moreover, the hollow $SnO_2$ microspheres have a better Coulomb efficiency during the whole measurements than that of commercial $SnO_2$ nanoparticles. The rate performance of hollow $SnO_2$ microspheres is summarised in the inset of Fig. 5*c*. The SIB cells based on hollow $SnO_2$ microspheres were cycled at four different current densities of 20, 50, 100 and 200 mA $g^{-1}$ in a voltage window of 0.05–2.0 V. As the current density increase, the charge/discharge capacity decrease gradually. Upon decreasing the current density from 200 to 20 mA $g^{-1}$, 69.0 and 77.6% capacity retentions are observed, corresponding to discharge and charge processes, respectively. This indicates that the hollow $SnO_2$ microspheres have an acceptable rate performance.

The kinetic property of hollow $SnO_2$ microspheres of fresh cells was measured by EIS (Fig. 6). The Nyquist plots indicated restrained semicircles in the high-to-medium frequencies, which relates to the charge transfer resistances ($R_{ct}$) for both anodes. The hollow $SnO_2$ microspheres have a lower charge transfer resistance than that of commercial $SnO_2$ nanoparticles, which can be attributed to the enlarged reactive area of hollow $SnO_2$ microspheres than that of commercial $SnO_2$, indicating faster $Na^+$ insertion/extraction kinetics across the electrode/electrolyte interface (Fig. 6). More important, the ordered $SnO_2$ microspheres could facilitate the charge transport/transfer compared with the disordered $SnO_2$ nanoparticles. The ex situ XRD pattern of the hollow $SnO_2$ microspheres after being fully discharged to 0.05 V shows that the $Na_{15}Sn_4$ were observed (Fig. 7), which coincide with the result obtained by Jiangfeng Qian.

The superior performance of hollow $SnO_2$ microspheres in SIBs was mainly attributed to the hollow structure with number of smaller nanoparticles. The spacing among smaller nanoparticle

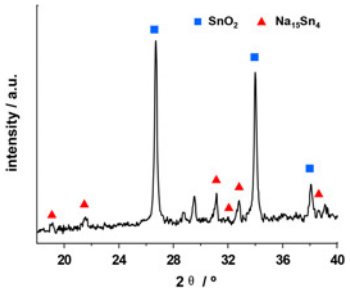


**Fig. 7** *Ex situ XRD pattern of the full discharged hollow $SnO_2$ microspheres*

size can shorten the diffusion distance of electrolyte ions and reduce the absolute stress/strain during cycling. Compared with the disordered commercial $SnO_2$ nanoparticles, the organised and hollow $SnO_2$ microspheres with mesopores and micropores not only can facilitate charge transfer between the electrode and electrolyte, improve electronic and ionic transports, but also can accommodate the volume change to enhance the cycling stability of $SnO_2$-based SIB anodes.

**4. Conclusions:** In summary, the hollow $SnO_2$ microspheres were obtained by a hydrothermal method with post-calcination in air. The hollow $SnO_2$ microspheres exhibit a sphere shape with an average diameter of 200–300 nm and an empty part in the core of it. There are small grains on the shell of the microspheres with an average size of 15.5 nm. This hollow $SnO_2$ microspheres show 3.3 times higher specific surface area than that of commercial $SnO_2$ nanoparticles. The electrochemical measurements show the hollow $SnO_2$ microspheres have around 3.3–3.6 times higher charge/discharge capacity and superior cycling stability and Coulomb efficiency than commercial $SnO_2$ nanoparticles when used as an anode material for SIBs. The organised and hollow $SnO_2$ microspheres with mesopores and micropores are the origin of the superior battery performances, which can provide more facility on charge transfer, mass transport and volume change. The hollow $SnO_2$ microspheres with excellent performance for SIBs might be a promising anode material for SIBs. The unique hollow microsphere structure can also be served as a good choice for SIBs nanomaterials construction.

**5. Acknowledgments:** This work was financially supported by Fundamental Research Funds for the Central Universities under grant nos. XDJK2016C005 and XDJK2015C061, China Postdoctoral Science Foundation under grant no. 2015M582495, Southwest University (Start Foundation for the Doctors, grant no. SWU112052), and Program for the Youth Talent in Science and Technology of Chongqing (grant no. cstc2014kjrc-qnrc50006).

## 6 References

[1] Sun J., Lee H.W., Pasta M., *ET AL.*: 'A phosphorene-graphene hybrid material as a high-capacity anode for sodium-ion batteries', *Nat. Nanotechnol.*, 2015, **10**, pp. 980–U184
[2] Balogun M.S., Luo Y., Qiu W.T., *ET AL.*: 'A review of carbon materials and their composites with alloy metals for sodium ion battery anodes', *Carbon*, 2016, **98**, pp. 162–178
[3] Li W.H., Yang Z.Z., Li M.S., *ET AL.*: 'Amorphous red phosphorus embedded in highly ordered mesoporous carbon with superior lithium and sodium storage capacity', *NanoLett.*, 2016, **16**, pp. 1546–1553
[4] Wang L.P., Yu L.H., Wang X., *ET AL.*: 'Recent developments in electrode materials for sodium-ion batteries', *J. Mater. Chem. A*, 2015, **3**, pp. 9353–9378
[5] Yabuuchi N., Kubota K., Dahbi M., *ET AL.*: 'Research development on sodium-ion batteries', *Chem. Rev.*, 2014, **114**, pp. 11636–11682
[6] Kim H., Kwon J.E., Lee B.N., *ET AL.*: 'High energy organic cathode for sodium rechargeable batteries', *Chem. Mater.*, 2015, **27**, pp. 7258–7264
[7] Fang Y.J., Xiao L.F., Ai X.P., *ET AL.*: 'Hierarchical carbon framework wrapped $Na_3V_2(PO_4)_{(3)}$ as a superior high-rate and extended lifespan cathode for sodium-ion batteries', *Adv. Mater.*, 2015, **27**, pp. 5895–5900
[8] Xiang X.D., Zhang K., Chen J.: 'Recent advances and prospects of cathode materials for sodium-ion batteries', *Adv. Mater.*, 2015, **27**, pp. 5343–5364
[9] Fernandez-Ropero A.J., Piernas-Munoz M.J., Castillo-Martinez E., *ET AL.*: 'Electrochemical characterization of $NaFe_2(CN)_{(6)}$ prussian blue as positive electrode for aqueous sodium-ion batteries', *Electrochim. Acta*, 2016, **210**, pp. 352–357
[10] Piernas-Munoz M.J., Castillo-Martinez E., Gomez-Camer J.L., *ET AL.*: 'Optimizing the electrolyte and binder composition for sodium prussian blue, $Na_{1-x}Fe_{x+(1/3)}(CN)_{(6)}$center dot $yH_{(2)}O$, as cathode in sodium ion batteries', *Electrochim. Acta*, 2016, **200**, pp. 123–130
[11] Zhao W.W., Tanaka A., Momosaki K., *ET AL.*: 'Enhanced electrochemical performance of Ti substituted P2-$Na_{2/3}Ni_{1/4}Mn_{3/4}O_2$ cathode material for sodium ion batteries', *Electrochim. Acta*, 2015, **170**, pp. 171–181
[12] Xie J.L., Yang P.P., He H.: 'Layered $Na_2Ti_2O_4(OH)_2$ and $K_2Ti_2O_4(OH)_2$ nanoarrays for Na/Li-ion intercalation systems: effect of ion size', *J. Electrochem. Soc.*, 2016, **163**, (10), pp. A1–A8
[13] Xiao L.F., Cao Y.L., Xiao J., *ET AL.*: 'High capacity, reversible alloying reactions in SnSb/C nanocomposites for Na-ion battery applications', *Chem. Commun.*, 2012, **48**, pp. 3321–3323
[14] Xia X., Obrovac M.N., Dahn J.R.: 'Comparison of the reactivity of $Na_xC_6$ and $Li_xC_6$ with non-aqueous solvents and electrolytes', *Electrochem. Solid State Lett.*, 2011, **14**, pp. A130–A1A3
[15] Wan F., Li Y.H., Liu D.H., *ET AL.*: 'Alkali-metal-ion-functionalized graphene oxide as a superior anode material for sodium-ion batteries', *Chem.-Eur. J.*, 2016, **22**, pp. 8152–8157
[16] Kim C., Lee K.Y., Kim I., *ET AL.*: 'Long-term cycling stability of porous Sn anode for sodium-ion batteries', *J. Power Sources*, 2016, **317**, pp. 153–158
[17] Cho E., Song K., Park M.H., *ET AL.*: 'SnS 3D flowers with superb kinetic properties for anodic use in next-generation sodium rechargeable batteries', *Small*, 2016, **12**, pp. 2510–2517
[18] Tang D.H., Huang Q.Q., Yi R., *ET AL.*: 'Room-temperature synthesis of mesoporous $Sn/SnO_2$ composite as anode for sodium-ion batteries', *Eur. J. Inorg. Chem.*, 2016, **2016**, pp. 1950–1954
[19] Shin H.S., Jung K.N., Jo Y.N., *ET AL.*: 'Tin phosphide-based anodes for sodium-ion batteries: synthesis via solvothermal transformation of Sn metal and phase-dependent Na storage performance', *Sci. Rep.*, 2016, **6**, p. 10
[20] Luo B., Qiu T.F., Ye D.L., *ET AL.*: 'Tin nanoparticles encapsulated in graphene backboned carbonaceous foams as high-performance anodes for lithium-ion and sodium-ion storage', *Nano Energy*, 2016, **22**, pp. 232–240
[21] Mao J.F., Fan X.L., Luo C., *ET AL.*: 'Building self-healing alloy architecture for stable sodium-ion battery anodes: a case study of tin anode materials', *ACS Appl. Mater. Interfaces*, 2016, **8**, pp. 7147–7155
[22] Bian H.D., Zhang J., Yuen M.F., *ET AL.*: 'Anodic nanoporous $SnO_2$ grown on Cu foils as superior binder-free Na-ion battery anodes', *J. Power Sources*, 2016, **307**, pp. 634–640
[23] Li Y.L., Wang J.J., Li X.F., *ET AL.*: 'Nitrogen-doped carbon nanotubes as cathode for lithium-air batteries', *Electrochem. Commun.*, 2011, **13**, pp. 668–672
[24] Gu M., Kushima A., Shao Y.Y., *ET AL.*: 'Probing the failure mechanism of $SnO_2$ nanowires for sodium-ion batteries', *Nano Lett.*, 2013, **13**, pp. 5203–5211
[25] Huang B., Li X., Pei Y., *ET AL.*: 'Novel carbon-encapsulated porous $SnO_2$ anode for lithium-ion batteries with much improved cyclic stability', *Small*, 2016, **12**, pp. 1945–1955
[26] Cheng Y.Y., Huang J.F., Li J.Y., *ET AL.*: 'Synergistic effect of the core-shell structured $Sn/SnO_2$/C ternary anode system with the improved sodium storage performance', *J. Power Sources*, 2016, **324**, pp. 447–454
[27] Li S.T., Wang Z.M., Liu J., *ET AL.*: 'Yolk-shell Sn@C eggette-like nanostructure: application in lithium-ion and sodium-ion batteries', *ACS Appl. Mater. Interfaces*, 2016, **8**, pp. 19438–19445




doi: 10.1049/mnl.2017.0304